Chemical Geology 560 (2021) 120018

Contents lists available at ScienceDirect

Chemical Geology

journal homepage: www.elsevier.com/locate/chemgeo

A multi-modal approach to measuring particulate iron speciation in buoyant hydrothermal plumes

Brandy D. Stewart [a], Jeffry V. Sorensen [a], Kathleen Wendt [a,b], Jason B. Sylvan [c], Christopher R. German [d], Karthik Anantharaman [e,f], Gregory J. Dick [e], John A. Breier [g], Brandy M. Toner [a,*]

[a] Department of Soil, Water, and Climate, University of Minnesota – Twin Cities, St. Paul, MN 55108, United States of America
[b] Institute of Geology, University of Innsbruck, Innrain 52, 6020 Innsbruck, Austria
[c] Department of Oceanography, Texas A & M University, College Station, TX, 77843, United States of America
[d] Woods Hole Oceanographic Institution, Woods Hole, MN, 02543, United States of America
[e] Department of Earth and Environmental Sciences, University of Michigan – Ann Arbor, Ann Arbor, MI, 48109, United States of America
[f] Department of Bacteriology, University of Wisconsin–Madison, Madison, WI, 53706, United States of America
[g] School of Earth, Environmental, and Marine Sciences, University of Texas Rio Grande Valley, Edinburg, TX, 78539, United States of America

ARTICLE INFO

Editor: B. Sherwood- Lollar

Keywords:
Hydrothermal vents
Iron
Fe
Thermodynamic modeling
Fe speciation
Synchrotron microprobe XANES
Synchrotron microprobe XRD

ABSTRACT

Processes active within buoyant hydrothermal plumes are expected to modulate the flux of elements, such as Fe, to the deep ocean; however, they are yet to be described in a comprehensive manner through observations or models. In this study, we compare observed particulate Fe (pFe) speciation with thermodynamic (equilibrium) reaction path modeling for three vent fields in the Eastern Lau Spreading Center (ELSC). At each site, particles were collected from the buoyant rising portion of hydrothermal plumes using in situ filtration with a Remotely Operated Vehicle. Filter bound particles were analyzed by synchrotron micro-probe X-ray fluorescence mapping (XRF), X-ray diffraction (XRD), XRF spectroscopy, and X-ray absorption near edge structure (XANES) spectroscopy at the Fe 1 s edge, as well as XRF-based chemical speciation mapping for Fe. For buoyant plumes of the ELSC, diversity in solid-state chemistry was high, and poorly crystalline, meta-stable phases were common. We demonstrate that to fully describe the crystalline-to-noncrystalline character of plume pFe, a multi-modal XRD-XANES analytical approach is needed. We found that an equilibrium modeling approach worked well for pyrite but performed poorly for important families of meta-stable pFe, namely Fe (oxyhydr)oxides and monosulfides. Based on our findings, we recommend future field expeditions strategically explore sites representing a diversity of site-specific conditions to better capture the full range of processes active in plumes. We also recommend development of kinetic models, as well as expansion of thermodynamic databases to better reflect the solid-state composition of plumes. These steps should allow oceanographers to understand the processes controlling Fe speciation in plumes well enough to create realistic models of hydrothermal fluxes to the ocean.

1. Introduction

Hydrothermal systems are globally distributed hydrologic features in which the flux of elements from the subseafloor to the base of the oceanic water column is modulated (German and Seyfried, 2014). At high temperature vents, physical, chemical, and microbiological processes active within buoyant hydrothermal plumes further regulate the gross flux of elements exiting the seafloor. Buoyant plumes are characterized by high dilution of vent fluids by entrained seawater (ca. 1:10,000) containing background dissolved and suspended materials, rise times of approximately one hour, and rise heights on the order of 200 m (Cron et al., 2020, German and Seyfried, 2014; Hoffman et al., 2018; Jiang and Breier 2014; Speer and Helfrich, 1995). Thus far, however, these turbulent, dynamic, and heterogeneous systems have eluded a global-scale understanding of their impact on ocean biogeochemistry (e.g. (Cron et al., 2020; Estapa et al., 2015; Mottl and McConachy, 1990; Sheik et al., 2015)). Based on current knowledge of neutrally buoyant plumes, it is likely that processes active within

* Corresponding author.
E-mail address: toner@umn.edu (B.M. Toner).

https://doi.org/10.1016/j.chemgeo.2020.120018
Received 25 August 2020; Received in revised form 24 November 2020; Accepted 2 December 2020
Available online 5 December 2020

buoyant plumes will govern key aspects of element fluxes, such as Fe, to the deep ocean, as well as speciation, potential for transport, and reactivity during transport (reviews by (Gartman and Findlay, 2020; Toner et al., 2015)). Recent work has demonstrated that Fe in the particulate size class (pFe; ca. > 200 nm) can be transported 100 s to 1000s of kilometers off axis (Fitzsimmons et al., 2017; Hoffman et al., 2018, 2020; Lam et al., 2018; Lee et al., 2018).

The analytical tools needed to measure the solid-state chemistry, or speciation, of hydrothermally derived pFe are well established (e.g. (Toner et al., 2015)). However, measuring the speciation of pFe, as well as other relevant size fractions, across a sampling of sufficiently diverse vent fields to arrive at a representative cross-section of global-scale ocean inputs represents a great challenge. Alternatively, modeling the speciation of Fe, and other hydrothermally sourced elements, produced within hydrothermal plumes could facilitate the extrapolation of plume processes to global scale ocean inputs; but plume mineral speciation models developed to date may not yet be robust enough for this task. What we present here is an integrative approach that combines direct observations of pFe speciation with high chemical resolution with thermodynamic modeling mineral speciation predications. Our goal is to develop a framework that can be used to develop, refine, and validate modeling approaches, which can then guide targeted field campaigns that could be used to test our understanding of hydrothermal plume processes across different physical and geological environments worldwide.

Thermodynamic modeling has been the principal approach used to date to predict mineral and dissolved phase chemical speciation within deep-sea hydrothermal plumes (Bowers and Taylor, 1985; Janecky and Seyfried, 1984; McCollom, 2000). Thermodynamic modeling is attractive because relatively rich databases and algorithms can be used to make predictions for the appropriate temperature and pressure ranges (Helgeson et al., 1978; Johnson et al., 1992; Shock et al., 1989). However, the mixing process and reaction path is very rapid with mixing from high to low temperatures occurring very near the vent within seconds to minutes (Jiang and Breier, 2014). Consequently, reaction kinetics are recognized as potentially limiting the accuracy of thermodynamic models in this process; but comparably rich kinetic speciation models appropriate for this temperature range have yet to be developed and tested. In addition, there has been little direct evidence as to how well thermodynamic modeling does or does not describe plume mineralogy. In this study, we compare thermodynamic predictions to observations in order to identify how the two differ.

Iron-bearing minerals present at equilibrium are those that draw down the activity of $Fe^{2+}_{(aq)}$ or $Fe^{3+}_{(aq)}$ to the greatest extent; these minerals are defined as stable phases. Any Fe-bearing minerals known to be present in samples from the field, but not predicted to be present at equilibrium, are meta-stable phases. The degree to which a thermodynamic model will faithfully predict mineral phases depends first on the thermodynamic database used in the model. Available thermodynamic parameters are biased toward well crystalline materials with no impurities or defects. Based on the results of studies of neutrally buoyant plumes (e.g. (Breier et al., 2012)), these characteristics (crystalline, no impurities, no defects) may be unrepresentative of many phases precipitating in buoyant plumes. Next, the quality of model predictions will depend on the degree to which equilibrium is achieved. For Fe-bearing phases that rapidly precipitate as a stable phase, thermodynamic modeling should provide a realistic view of pFe speciation. However, for Fe-bearing phases that come to equilibrium slowly, relative to mixing and transport times, thermodynamic modeling may fail to predict the actual (meta-stable) pFe phases formed in buoyant plumes.

Particulate Fe speciation is complex for neutrally buoyant plumes and a continuum of crystalline to non-crystalline phases are observed (Breier et al., 2012; Hoffman et al., 2018; (Toner et al., 2009)). The gold standard of phase identification is X-ray diffraction (XRD), and this mode of detection relies on Bragg diffraction phenomena resulting from repeating structural motifs. In other words, it relies on the well-crystalline character of solids. For poorly crystalline materials—or materials with nanometer size, impurities, or defects—XRD typically fails to produce signals that are decipherable in complex materials like hydrothermal plume particles. For poorly crystalline phases, X-ray absorption spectroscopy (XAS) can be used to accomplish phase identification by observing the valence state and local coordination environment for a specific element. Since this approach does not rely on crystallinity, it can detect poorly crystalline phases. However, XAS requires a geochemically relevant reference database for data analysis and detects just one element at a time (e.g. all Fe-bearing phases present).

Hydrothermal plumes are known to produce two major families of Fe-bearing minerals or phases, Fe sulfides and Fe (oxyhydr)oxides (oxides, hydroxides, and oxyhydroxides) (Breier et al., 2012; Campbell, 1991; Cowen et al., 1986; Feely et al., 1994; Feely et al., 1987; Gartman et al., 2019; (Toner et al., 2009); Yucel et al., 2011). While both families have exemplary crystalline members, e.g. pyrite (FeS_2) and goethite (α-FeOOH), both also contain variable stoichiometry and poorly crystalline members, e.g. pyrrhotite ($Fe_{1-x}S$; x = 0–0.17) and ferrihydrite ($Fe_2O_{3-0.5y}(OH)_y \cdot nH_2O$; y = 0–1.96; n = 0.82–1.14) (Yu et al., 2002). Therefore, a complete understanding of pFe in buoyant plumes requires more than one analytical approach.

In this study, we have measured pFe speciation within buoyant hydrothermal plumes and determined the degree to which pFe speciation is represented accurately by a thermodynamic modeling approach. For buoyant plumes at the Kilo Moana, ABE, and Mariner vent fields of the Eastern Lau Spreading Center (ELSC), we used multiple analytical approaches (multi-modal) to observe different characteristics of the pFe present in our samples. Specifically, synchrotron micro-probe XRD and XAS were used to measure the solid-state chemistry of particles retained on 0.8 μm pore-size filters. The pFe results, composed of both crystalline and poorly crystalline Fe-bearing phases, were then compared to thermodynamic modeling results. We use the lessons learned from that comparison to propose several best-practices that should help our research community build a foundation for modeling hydrothermal Fe fluxes to the ocean in terms of field studies, analytical observations, and model development.

2. Methods and Materials

2.1. Site Description

The Lau Basin is located adjacent to the Australian-Pacific convergent plate boundary in the South Pacific Ocean. Back-arc spreading along the length of the Lau Basin is dominated by the Eastern Lau Spreading Center (ELSC) which extends ~400 km, North to South, and can be sub-divided into three morphologically distinct ridge sections: the Northern and Central Eastern Lau Spreading Centers (N-ELSC, C-ELSC), and the Valu Fa Ridge (VFR) (Ferrini et al., 2008). Each section of this back-arc spreading center is characterized by differing spreading rates and host geology which vary systematically from south to north as separation from the Tonga volcanic arc increases (Martinez et al., 2006). The N-ELSC begins at 19°20′S and extends to 20°32′S with a spreading rate of 96 mm/yr. The seafloor of the N-ELSC lies at water depths of 2500-2000 m and is covered uniformly by pillow lavas. The C-ELSC is defined as the area from 20°32′S to 21°26′S. It exhibits spreading rates that decrease from 75 mm/yr to 61 mm/yr from North to South and the seafloor is covered by pillow and lobate lava. Axial magma chambers underlie much of the ELSC and reach a depth of 2–2.5 km below the seafloor at the central-ELSC (Jacobs et al., 2007). The southernmost segment from 21°26′S to 22°45′S, the Valu Fa Ridge, is the shallowest portion of the ELSC. Spreading rate along the VFR decreases from 61 to 31 mm/yr from north to south.

During hydrothermal exploration along the ELSC under the auspices of the Ridge 2000 program, multiple hydrothermal plume anomalies were detected, six of which were then tracked to their source using the ABE autonomous underwater vehicle for follow-on detailed process

studies (Ferrini et al., 2008; German et al., 2008; Martinez et al., 2006). Buoyant plume process studies conducted at three of those sites, the Kilo Moana, ABE, and Mariner revealed buoyant plumes with strong contributions from background seawater add (Sheik et al., 2015).

2.1.1. Kilo Moana Vent Field (20°3′11.52″S, 176°7′53.76″W)

Kilo Moana is located 500 m west of the northern-ELSC spreading axis on a slightly asymmetric bathymetric high (Ferrini et al., 2008). Temperatures at Kilo Moana reach up to 333 °C at water depths of 2620 m. The Kilo Moana vent field is surrounded by basaltic substrate host rock dominated by pillow lava and little sediment cover (Bezos et al., 2009). Bathymetric maps reveal two wide volcanic domes that are cross cut by two well-defined fissures running north-south. The western fissure is 9 m deep and 4–20 m wide while the eastern fissure is 10 m deep and 5 m wide. Hydrothermal vent structures are evident adjacent to and at the intersection of both fissures. Hydrothermal activity extends north-south for ~130 m with three localized areas of high-temperature venting and diffuse flow. Kilo Moana chimneys are ~5 m tall with coalesced pipes, cactus-like protrusions, and beehive-like structures with chalcopyrite (CuFeS) and wurtzite ((Zn,Fe)S) lined conduits (Evans et al., 2017). The end member vent fluids from the Kilo Moana vent field have a pH of 3.5 and concentrations of dissolved sulfide, Fe, and Mn of 5.7, 3, and 0.6 mmol/kg seawater, respectively (Mottl et al., 2011).

2.1.2. ABE Vent Field (20°45′42.84″S, 176°11′27.6″W)

Located in the central-ELSC region, the ABE vent field is 600 m west of the spreading axis at a water depth of 2220 m and is characterized by vent fluids with temperatures up to 309 °C. ABE is surrounded by pillow and lobate lava host rock with moderate sediment cover and is close to a northeast-southwest oriented fault with parallel steps (Ferrini et al., 2008). At least three identifiable lava flow fronts intersect faulting regions generating conditions favorable to hydrothermal activity. ABE consists of three areas of active venting spaced ~85 m apart along the dominant fault. Similar to Kilo Moana, vent fluids create chalcopyrite and wurtzite lined conduits in small, branched chimneys (Evans et al., 2017). The end member vent fluids have a pH of 4.5 and dissolved sulfide, Fe, and Mn concentrations of 3, 0.2, and 0.3 mmol/kg seawater, respectively (Mottl et al., 2011).

2.1.3. Mariner Vent Field (22°10′48″S, 176°36′6.12″W)

Located along on the eastern limb of an overlapping spreading center on the Valu Fa Ridge section of the southern-ELSC, Mariner is the shallowest vent field at 1910 m water depth. In contrast to Kilo Moana and ABE, local faults and fissures are notably absent at Mariner. Heavy sediment cover and felsic host rock, ranging from basalt enriched with lithophile elements to andesite, surrounds Mariner (Jacobs et al., 2007). The vent field is dominated by numerous flat-topped and crater lava domes. Venting at Mariner occurs from the base and sides of 10 to 25 m tall, narrow pinnacle structures. High temperature fluids up to 363 °C exit through chalcopyrite-lined conduits and porous beehive structures. Higher temperatures combined with the absence of faulting and abundance of magmatic carbon dioxide, suggest hydrothermal activity at the Mariner vent field is the result of magmatic rather than faulting processes (Evans et al., 2017; Mottl et al., 2011). The end member vent fluids have a pH of 2.6 and dissolved sulfide, Fe, and Mn concentrations of 6, 11, and 5.6 mmol/kg seawater, respectively (Mottl et al., 2011).

2.2. Sample collection

Samples were collected on two cruises of the *R/V Thompson* to the Lau Basin (TN235 and TN236) in 2009. Plume particles were collected from the buoyant plume of three vent fields using the *ROV Jason II* and a suspended-particle rosette (SUPR) multi-sampler capable of collecting 24 discrete samples on 0.8 μm polycarbonate membrane filters (Breier et al., 2009). A hose extension was fitted to the *ROV Jason* to allow for sampling fluids within the buoyant plume. Variability in particle concentration, caused by turbulence within the plume as it rises, necessitated collection times from 10 to 30 min/sample. Sampling was conducted by: (1) approaching a vent structure from the side; (2) collecting a near bottom background (NBB) sample; (3) placing the sampling hose above the vent and within the buoyant plume and collecting a sample; (4) *the ROV* was then piloted vertically within the buoyant plume (using the ROV's auto x-y positioning capabilities) to the next requested sampling height, using the ROV's altimeter to monitor height above the seafloor.

To preclude contamination of our samples, all sampling components were cleaned with a 5% ethanol / 5% HCl (Seastar) solution. Plasticware was rinsed with MilliQ purified water and leached with 10% HCl (Seastar) at pH 2. Once aboard ship, filter bound samples were recovered from the SUPR sampler in an argon purged glovebox, packed in plastic vacuum containers within the same argon purged glovebox, and stored and shipped frozen.

Near-bottom background (NBB) samples were collected at the ABE and Kilo Moana vent sites near the seafloor at the outset of the plume profile prior to sampling within the rising plume (Fig. 1). Samples were collected in four locations at the Kilo Moana vent: two were within the buoyant plume at 0.5 m and 200 m plume elevation and two were background samples, one from the water column above the plume (above plume background (APB)) and one from the bottom water near the vent (NBB). At the ABE vent site, samples were collected within the buoyant plume at 1.5 m, 10 m, 40 m, and 200 m plume elevation, as well as above plume background and near bottom background samples (Fig. 1). Finally, at the Mariner vent field, two samples were collected from within the buoyant plume at 0.5 m and 25 m plume elevation.

2.3. Bulk Geochemistry

Particulate filter samples were collected with 37 mm diameter, 0.8 μm poresize polycarbonate membranes (GE Osmonics). Filter membranes were completely digested in 30 mL acid cleaned perfluoroalkoxy vials (Savillex) using the following procedure based on Bowie et al. (2010). Each filter was added to a digestion vial with 2 ml concentrated nitric acid. The vials were capped and heated at 110 °C for 4 h. After cooling 0.5 mL of concentrated hydrofluoric acid was added to each vial. The vials were capped and heated at 110 °C for 4 h. The vials were then uncapped and heated at 120 °C to dryness. An additional 100 μL of concentrated nitric acid was added and similarly taken to dryness to facilitate evaporation of the hydrofluoric acid. After cooling, the digested sample was taken back into solution by adding 3 mL of a 3%

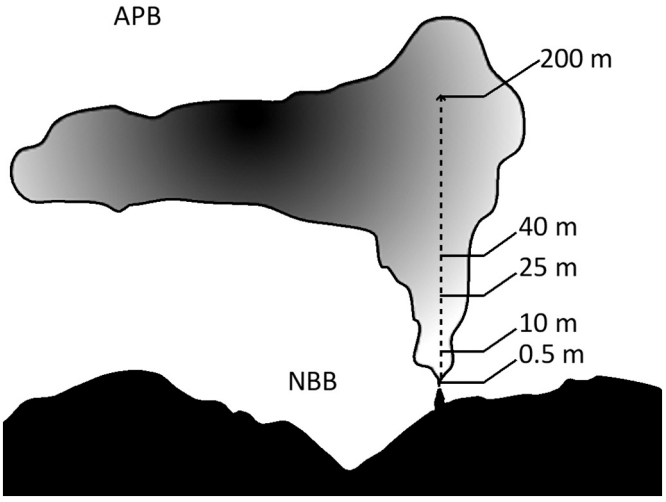

Fig. 1. Schematic of buoyant hydrothermal plume showing plume elevation (in meters) and approximate location of sampling at ABE vent field, including the near bottom background (NBB) and above plume background (APB).

nitric acid matrix. The vials were capped and heated for 1 h at 60 °C. This process resulted in the complete digestion of visible particles and in most cases the filter, in the few cases where residual filter material (<1% of the whole filter) remained it was removed by filtration of the digest solution. All acids were trace metal grade (Optima, Fisher Scientific). Vials were heated in a temperature-controlled hot plate (Qblock, Questron Technologies). Aliquots of sample digest, at a 1:10 dilution, were analyzed for Fe on a Varian 730-ES axial spectrometer by Activation Laboratories. External standards were used for instrument calibration. Digestion and analysis were both monitored by processing and comparing filter and acid blanks, geostandards (MAG1 & BHVO), and our internal sulfide standards by these same methods (Breier et al., 2012; Govindarajan, 1994).

2.4. Synchrotron X-ray microprobe analysis of particles

All synchrotron analyses for this project were analyzed at the Advanced Light Source, Lawrence Berkeley National Laboratory, using the hard X-ray microprobe beamline (BL) 10.3.2 (Marcus et al., 2004). Approximately one hour prior to each analysis, a sample-bearing filter was defrosted and mounted to an aluminum sample holder. During the X-ray microprobe measurements, buoyant plume particles were exposed to ambient temperature and atmosphere. After analysis, samples were returned to an argon filled glove box, sealed into plastic bags before being heat-sealed in mylar pouches with oxygen scrubbers (Anaero Pack, Mitsubishi Gas Chemical Co., Inc.) and re-frozen prior to return to the laboratory at the University of Minnesota.

Data collection at BL 10.3.2 for filter-bound plume particles had the following task flow: (1) X-ray fluorescence (XRF) mapping at multiple energies to determine the spatial distribution of elements in the particles; (2) point X-ray absorption near edge structure (XANES).

measurements within XRF mapped areas at the As, Fe, Mn, and V 1 s (or K-edge) absorption edges to define particle chemistry; (3) point X-ray diffraction (XRD) and point XRF spectra were measured for particles within the XRF mapped areas; (4) Fe speciation mapping to quantify the relative abundance of Fe species; and (5) additional point Fe XANES to validate the fits to the speciation map.

2.4.1. X-ray fluorescence mapping

X-ray fluorescence mapping typically included: (1) an "As map" with incident energy set to PbL3–50, or 12,985 eV, that provided Fe, Ni, Cu, Zn, and As distributions; (2) a "Mn map" with incident energy set to FeK-50, or 7062 eV, that provided Mn distribution without interference from Fe Kα fluorescence emission; (3) a "V map" which was generated by subtracting a VK-50, or 5415 eV map from a VK + 100, or 5565 eV to distinguish V Kα from Ti Kβ fluorescence emission; and (4) maps for Si, S, Cl, K, and Ca that were typically obtained from the lowest energy map collected (e.g. the below-V map at 5415 eV). Individual XRF maps were deadtime corrected, aligned, and channels of interest were added to a single composite map using custom beamline software (Marcus et al., 2004).

2.4.2. Point XANES

X-ray absorption near edge structure spectroscopy was conducted at the V, Mn, Fe, and As K (or 1 s) absorption edges using a 7-element germanium detector in fluorescence mode. The monochromator energy calibration was set with the inflection point of a scan of V foil at 5463.76 eV, Mn foil at 6536.95 eV, and Fe foil at 7110.75 eV, or set at the white line maximum of a scan of sodium arsenate powder at 11,875 eV. The V, Mn, Fe, and As XANES spectra were collected in the range 5350–5720 eV, 6439–6838 eV, 7011–7414 eV, and 11,769–12,179 eV, respectively. Individual scans collected at the same sample location were examined for changes in line-shape and peak position, and no photon-induced sample damage was observed.

2.4.3. XANES data analysis

Spectra were deadtime corrected, energy calibrated, and averaged using custom beamline software (Marcus et al., 2004). The software program Athena was used to perform pre-edge subtraction and post-edge normalization (Ravel and Newville, 2005). Normalized spectra were subjected to linear combination fitting (LCF) with reference spectra using custom beamline software (Marcus et al., 2004) as described in (Breier et al., 2012). For Fe, the reference spectra database has 94 entries (Hansel et al., 2003; Marcus et al., 2008; Toner et al., 2012a) (Table S1 displays all LCF results). For As, the reference spectral library consists of 20 unpublished entries (Nicholas et al., 2017). For Mn, the peak positions were compared to published values for Mn(II), Mn(III), and Mn(IV) (Bargar et al., 2000). For V, the peak positions were compared to published values for 19 V species (Shafer et al., 2011). The LCF results were ranked using the normalized sum-squares (NSS) parameter:

$$NSS = 100 \times \left\{ \sum \left(\mu_{exp} - \mu_{fit}\right)^2 \Big/ \sum \left(\mu_{exp}\right)^2 \right\}$$

Where μ represents the normalized absorbance of the experimental (μ_{exp}) and fit (μ_{fit}). Additional components were added to a fit when the change resulted in an improvement in the *NSS* by ε 10%. It is important to note that LCF analysis of experimental data with reference spectra is dependent on the degree to which the references represent the chemistry of the samples. The Fe XANES database used in this study is robust in that it covers a wide range of relevant Fe-bearing solids. Despite this, the appearance of a specific reference, such as "hypersthene" (a metamorphic inosilicate within the enstatite-ferrosilite solid solution series), in the best linear combination fit (LCF) does not mean that hypersthene is present in the sample. The interpretation is confounded by the fact that hypersthene does not have a unique chemical formula and the Fe XANES spectra are rarely diagnostic for a specific phase. The soundest interpretation is that the sample contains Fe in a hypersthene-like chemical state (valence plus local coordination environment). Therefore, in this study, we use a post-LCF binning process. In the example of hypersthene, it would be binned as a primary "silicate".

Iron XANES spectra were binned after LCF into six speciation categories: (1) "Fe(0)" is native or metallic Fe and is considered to be a shipboard contaminant (Hoffman et al. 2020); (2) "Sulfide" includes all Fe-bearing sulfide minerals such as pyrite and pyrrhotite; (3) "Silicate" includes any Fe-bearing primary silicate mineral having Fe(II) and/or Fe (III) such as chlorite and andradite; (4) "Fe(II)" includes any non-sulfide or non-silicate phases such as ilmenite; (5) "Fe(II,III)" are mixed valence (oxyhydr)oxides of Fe, such as magnetite and green rust; and (6) "Fe (III)" includes Fe(III) (oxyhydr)oxides and secondary Fe(III) phyllosilicates. A complete list of all reference spectra used in LCF and the corresponding Fe species bin are displayed in Table S2.

2.4.4. X-ray diffraction

Microprobe XRD patterns were collected at an incident energy of 17 keV (λ = 0.729 Å) with 240-s exposure and a spot size of 6 × 11 μm. The XRD patterns were radially integrated to obtain profiles of intensity versus 2θ using the freeware Fit2D after calibration of sample-to-detector distance with data from an Al_2O_3 (alumina) standard (Hammersley et al., 1996). Background filter XRD scans were collected.

Sampled XRD patterns underwent JADE software peak analysis (Materials Data Inc). Background filter XRD patterns were displayed and individually subtracted from each sample pattern. Additional background noise detected by JADE was subtracted to produce a uniform baseline for the XRD patterns. Sampled patterns underwent peak identification using the mineral standards of MDI-500 and AMCS databases to produce a list of possible standard-to-sample mineral matches. The chemistry filter function in JADE was used to search for matches containing elements identified by XRF spectra collected at the same location as the XRD pattern. Each listed match was quantitatively assigned a Figure of Merit (FOM) number based on the quality of match where an

FOM number (or rating) of zero represents a perfect sample-to-standard correlation and an FOM $\geq$ 25 represents an imperfect standard-to-sample match due to missing, oversized, or offset peaks from pattern.

Analyzing XRD mineral data from natural samples poses a number of challenges and standard protocols for XRD pattern identification did not work well for most of our data; therefore, we developed a *best-fit* point system to rank potential matches. We assigned two points to potential minerals with an assigned FOM of 25.0 or below and one point to potential minerals with an assigned FOM 25.1 or above. One additional point was given to potential minerals that corresponded with XRF identified elements. A maximum *best-fit* score of 3 represents a highly confident mineral identification (additional details on XRD data collection and point system in Supporting Information).

2.4.5. Chemical mapping

An Fe speciation mapping protocol developed for hydrothermal plume particles at the East Pacific Rise (Toner et al., 2012a; Toner et al., 2015; (Toner et al., 2014)) was applied to the ELSC samples. The method has components similar to chemical/speciation/multi-energy mapping methods developed for As, (Nicholas et al., 2017), Fe (Lam et al., 2018; Mayhew et al., 2011; Toner et al., 2012b), and S (Zeng et al., 2013). Briefly, multiple XRF maps were collected from sample areas with energies spanning the Fe K absorption edge. The number of XRF maps, and the incident energy for each, was selected based on: 1) the Fe species observed in point XANES spectra; and 2) the degree to which the energies distinguish among the species present. This selection process was aided by a custom beamline program called *Chemical Map Error Estimator* (Nicholas et al., 2017; Zeng et al., 2013).

For the ELSC plume particles, point XANES indicated that 8 incident energies were needed to describe the Fe species present: 7110, 7113.3, 7120.9, 7125, 7127.5, 7129.2, 7132.5, and 7350 eV. The XRF maps were deadtime corrected, registered, and compiled into a single file that is referred to hereafter as a "speciation map". All speciation maps were fit pixel-by-pixel using LCF with reference spectra and a materials blank. The LCF output was binned into three Fe species categories: (1) "Fe sulfide" which includes all Fe-bearing sulfide minerals; (2) "Fe(II)" includes all non-sulfide Fe(II)-bearing phases including Fe(II) silicates; and (3) "Fe(III)" which includes all Fe(III)-bearing phases such as Fe(III) oxyhydroxides and Fe(III)-bearing silicates.

The resulting speciation maps are three-dimensional datasets composed of an x-y plane representing the surface of the sample filter and a z-axis at every pixel representing an absorption profile as a function of incident energy. These absorption profiles are XANES spectra with low spectral resolution so the fit results are binned into species groups. For example, we cannot distinguish among Fe(III) oxyhydroxides with our speciation maps (e.g. goethite from akaganeite), but we can distinguish Fe-sulfides from Fe(III) oxyhydroxides (e.g. pyrite from any of the oxyhydroxides). Species bins that reflect our ability to distinguish different Fe species groups were used. Point Fe XANES data were then collected at select points within the speciation map area to ground-truth the fit.

2.5. Geochemical reaction path modeling

Equilibrium thermodynamic reaction path modeling was used to predict chemical concentrations, activity coefficients, and mineral saturation states during the mixing of seawater with end member vent fluid from the A1 vent at the ABE hydrothermal field, the MA1 vent at the Mariner hydrothermal field, and the KM1 vent at the Kilo Moana hydrothermal field (Mottl et al., 2011) (Table S4). Our approach follows those of past studies (Bowers and Taylor, 1985; Janecky and Seyfried, 1984; McCollom 2000); and, our specific plume thermodynamic model implementation has been described previously (Anantharaman et al., 2013; Anantharaman et al., 2014; Breier et al., 2012). The following is a brief description of model aspects specific to this study.

Vent fluid compositions (Table S4) are based on measurements made from samples collected in 2005 (Mottl et al., 2011; Seewald et al., 2005). Vent fluid concentrations for Cu, Zn, and Ba are based on EPR 21° N for lack of more relevant data (Von Damm et al., 1985). In situ pH was calculated from measurements of pH at 25 °C using an equilibrium reaction path model that increased the temperature of the measured fluid to the original vent fluid temperature. Background seawater dissolved O_2 concentrations are based on WOCE measurements from section P06 (Talley, 2007). Background seawater dissolved H_2 is assumed to be controlled by atmospheric equilibrium; this is consistent with previous findings for H_2 in the Atlantic Ocean (Conrad and Seiler, 1988). Aspects of Lau vent chemistry have been measured at other times but not in sufficiently complete a set of parameters as the vent chemistry and background seawater chemistry selected for this model. The data selected for this model predates this study; actual chemistries for these parameters may have differed during this study.

Reaction path modeling was performed with REACT, part of the Geochemist's Workbench package. The plume reaction path is modeled through a mixing process that ends at a vent fluid to seawater dilution of 1 part in 10,000, encompassing dilutions across the full rise-height of a buoyant hydrothermal plume. Precipitated minerals were allowed to dissolve and their constituents to re-precipitate based on thermodynamic equilibrium constraints. The thermodynamic data upon which this model is based was predicted by SUPCRT95 (Johnson et al., 1992) for the temperature range of 1–425 °C (specifically 1, 25, 60, 100, 225, 290, 350, and 425 °C) and a pressure of 500 bar, a pressure and temperature range that encompasses all known deep sea vents. SUPCRT95 uses previously published thermodynamic data for minerals, gases, and aqueous species (Helgeson et al., 1978; McCollom and Shock, 1997; Saccocia and Seyfried, 1994; Shock and Helgeson, 1990; Shock et al., 1989; Shock et al., 1997; Sverjensky et al., 1997). Thermodynamic data for pyrolusite, bixbyite, hausmannite, and marcasite were added from Robie et al. (1979) and thermodynamic data for $Fe(OH)_3$ were added from Wagman et al. (1982). Additional H_2-producing reactions for the formation of elemental S, bornite, pyrite, chalcopyrite, and covellite were also added (McCollom, 2000). The B-dot activity model was used (Helgeson, 1969; Helgeson and Kirkham, 1974). Temperature dependent activity coefficients were used for aqueous CO_2 and water in a NaCl solution (Bethke, 2007; Cleverley and Bastrakov, 2005; Drummond, 1981). A general limitation of REACT is that it does not predict the thermodynamic behavior of solid solutions. Thus minerals such as sphalerite, pyrrhotite, chalcopyrite, and isocubanite are treated as separate phases with ideal stoichiometry. This may influence the predicted plume mineral assemblage.

Following assumptions used in previous models, HS^-/SO_4^{2-} equilibration was suppressed on the basis that this reaction is kinetically inhibited on the short timescales of transport in the rising plume. For similar reasons, the precipitation of quartz and other silicate minerals were also suppressed in previous studies. Here, however, we consider the potential precipitation of trace and non-equilibrium minerals as well as equilibrium minerals. For this reason, all minerals were allowed to precipitate when thermodynamically predicted to do so. The ratio of the ion activity product and the thermodynamic solubility product were predicted for all minerals in the model so that the saturation state of trace and minor minerals could be evaluated. Precipitated minerals were allowed to dissolve and their constituents to re-precipitate based on thermodynamic equilibrium constraints. Consequently, a summation of minerals present at any point in the reaction path would only represent a subset of all minerals that precipitate during the process; these values can be mutually exclusive (e.g., pyrite, magnetite, and Fe hydroxide) and should not be integrated along the reaction path. To summarize all of the minerals that precipitate during the reaction path, Table S5 lists the set of minerals that achieve a saturation index of 1 and achieve an equilibrium state along the modeled reaction path (Supporting Information). In addition, Table S5 also lists those minerals that achieve lower saturation indices because they have the potential to precipitate if plume physical or chemical conditions are different or where kinetic

inhibitions prevent other minerals from precipitating.

3. Results

Particle chemistry (> 0.8 μm) in buoyant plumes along the ELSC was investigated at the Mariner, ABE, and Kilo Moana vent fields. Buoyant plume samples from each location were collected by in situ filtration and bulk major element concentration was measured by digestion and ICP-MS. Fig. 1 shows a schematic of the ABE plume indicating elevations above the vent where samples were collected and approximate location of near bottom background (NBB) and above plume background (APB) samples. Mariner and Kilo Moana vent fields were sampled in a similar way. Total particulate iron concentrations ranged from <4 nmol Fe/kg seawater in above plume background (APB) samples to 204 nmol Fe/kg at a plume elevation of 0.5 m at Mariner (Table 1). Within the ABE plume, particulate Fe concentrations decreased from 19 nmol Fe/kg near the source of the plume (1.5 m) to 4 nmol Fe/kg at a plume elevation of 200 m above the vent (Table 1).

3.1. Particulate Fe chemical speciation

In this study, we measure pFe specation using two different synchrotron X-ray microprobe approaches, point XANES and chemical mapping, that rely on X-ray absorption phenomena (Toner et al., 2015; (Toner et al., 2014); Toner et al., 2012b). In practice, these two approaches are applied iteratively with the findings of one observation type informing data collection and analysis in the other (Nicholas et al., 2017). The point XANES data, in conjunction with multi-element XRF mapping, are used to generate a complete list of Fe species present in the filter-bound sample. Points for XANES analysis are chosen to query Fe in different chemical environments according to co-located elements (identified from XRF maps) or different Fe species (identified by chemical maps). This means that the points are not selected at random to quantify the distribution of Fe species on the filter. Rather, the goal was to discover the number of different types of Fe species present in the sample and collect high quality spectra for phase identification of those types. The chemical mapping approach trades spectral, and therefore chemical, resolution for a larger number of observations. The strength of the chemical mapping is that the true quantities of Fe species present can be measured for a filter-bound sample. Using these two complementary approaches together, a typical experiment for a filter-bound sample could include tens of point XANES with high spectral resolution, and a chemical map with 100,000+ observations (i.e. pixels) with low spectral resolution. The purpose of pairing point XANES observations (high spectral resolution) with chemical mapping (low spectral resolution but large number of points queried) is to overcome the quantification issue caused by non-random selection of XANES points. If the number of XANES points is increased, then the Fe speciation measured by XANES will converge with that observed with chemical mapping. Similarly, if the number of incident energies in a chemical map is increased, then the specificity of the Fe species bins, and the overall quality of phase identification, will converge with the level of detail obtained by point XANES.

Point Fe XANES were collected and analyzed for solid particulate samples from buoyant plumes at the ABE, Kilo Moana, and Mariner ventfields. Linear combination fitting results from spectra were pooled and binned to produce a data set with 6 different Fe speciation categories: Fe (0), Fe-sulfide, Fe-silicate, Fe(II), Fe(II/III), and Fe(III), and their *estimated* relative proportion within a given sample. Iron speciation mapping was used for the same filter- bound samples to provide an actual *measured* relative proportion of three Fe species (Fe(II), Fe(III), and Fe-sulfide; additional details in Methods).

3.1.1. Comparison across sites at 0.5 m and 200 m

Results from point Fe XANES are presented in Fig. 2 for the Mariner, Kilo Moana, and ABE plumes at 0.5 m (Mariner and Kilo Moana) and 1.5 m (ABE) and for the Kilo Moana and ABE plumes at 200 m plume elevation. At the lowest plume elevations, Fe in all three plumes is predominately in the form of Fe-sulfide. Kilo Moana has the highest sulfide proportion at >80 mol% (per atom basis), while the proportion at both Mariner and ABE lies closer to 50% (per atom basis). Mariner is the only location with a significant proportion of Fe-silicates, while the ABE plume is the only one of the three with a significant pool of non-sulfide Fe(II) near vent. Finally Kilo Moana is the sole plume with a sizeable proportion of Fe(II/III) mixed valence minerals. Both the Mariner and ABE plumes at near vent elevation have an Fe(III) proportion of 15–20%, while interestingly there is no measurable Fe(III) at 1.5 m plume elevation at the Kilo Moana location (Fig. 2, Table 1).

Moving away from the source of the plume to an elevation of 200 m, the relative proportions of pFe shift in both the Kilo Moana and ABE buoyant plumes. The Fe-sulfide component decreases from greater than 50% of the total Fe to 25% and 35% in the Kilo Moana and ABE plumes, respectively (all % per atom basis). This coincides with an increase in the silicate and Fe(III) fractions in the Kilo Moana plume and a sizeable increase in Fe(III) minerals, from 15% to >50% (per atom basis), in the ABE plume (Fig. 2).

Similarly, results from Fe speciation chemical mapping (Figs. S3–5) indicate an increase in the proportion of Fe(III) and a decrease in the proportion of reduced Fe (Fe(II) and/or Fe-sulfide) between near vent and a plume height of 200 m for both the Kilo Moana and ABE plumes (Table 1). For example, in the ABE plume the Fe(III) proportion increases from 33 to 39% while the Fe(II) concentration decreases by 50% from 14 to 7% and the Fe-sulfide proportion remains roughly consistent at 52–54% (per atom basis). The speciation differs slightly in the Kilo

Table 1
Proportion of Fe-Sulfide, Fe(II) and Fe(III) for all sampling locations and plume elevations based on chemical mapping measurements.

Vent Field	Buoyant Plume Location	Plume Elevation (m)	Proportion Fe-Sulfide	Proportion Fe(II)	Proportion Fe(III)	pFe (nmol Fe/kg seawater)[c]	Temp (deg C)
ABE	NBB[a]	0	0.40	0.08	0.52	10.6	309.00
ABE	1.5 m	1.5	0.52	0.14	0.33	18.9	
ABE	10 m	10	0.13	0.09	0.78	4.21	
ABE	40 m	40	0.36	0.13	0.51	3.16	
ABE	200 m	200	0.54	0.07	0.39	3.86	
ABE	APB[b]	300	0.05	0.04	0.91	1.06	
Kilo Moana	NBB	0	0.23	0.06	0.71	18	333.00
Kilo Moana	0.5 m	0.5	0.35	0.11	0.54	35.8	
Kilo Moana	200 m	200	0.15	0.10	0.74	3.16	
Kilo Moana	APB	300	0.15	0.33	0.52	3.81	
Mariner	0.5 m	0.5	0.03	0.08	0.87	204	334.00
Mariner	25 m	25	0.24	0.27	0.48	10.5	

[a] Near bottom background.
[b] Above plume background.
[c] Total particulate Fe concentration (pFe) was measured by ICP-OES after digestion of filter solids.

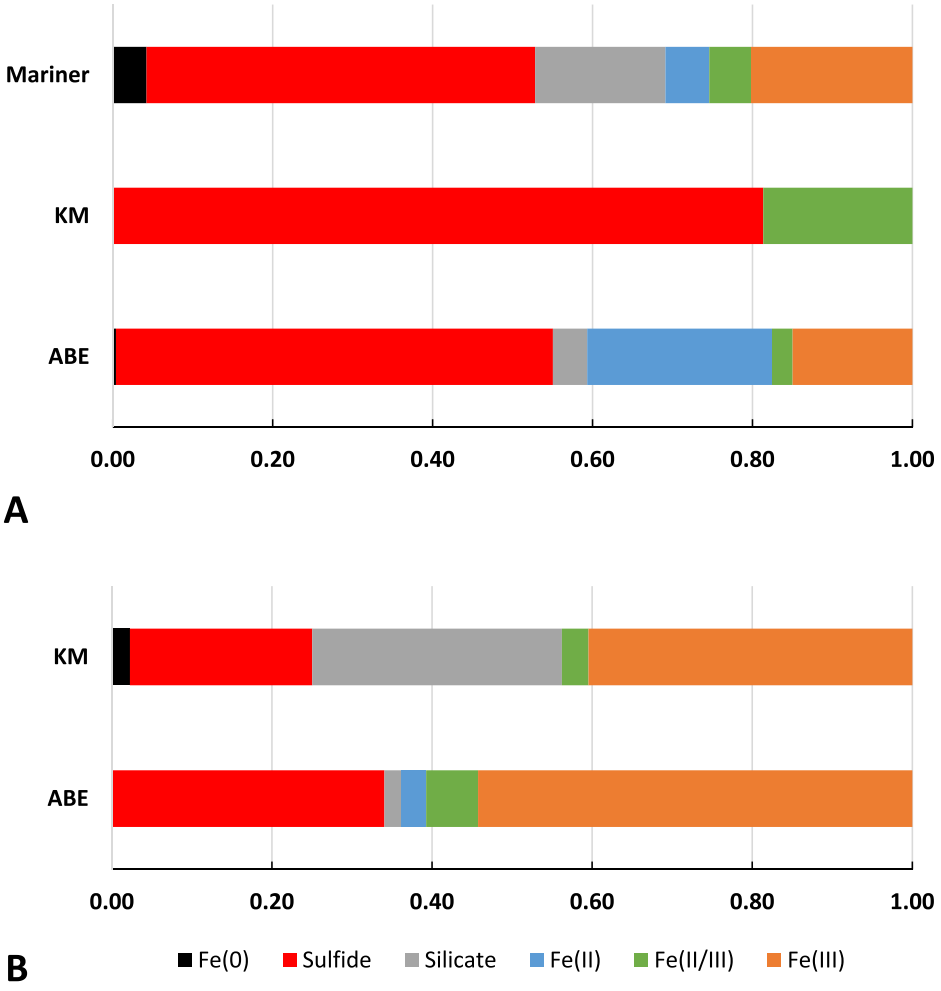

Fig. 2. Results from point X-ray absorption near edge structure (XANES) spectra showing difference in particulate Fe speciation among locations, the Kilo Moana, ABE, and Mariner vent fields, for a given plume elevation. A) 0.5/1.5 m and B) 200 m above the vent and within the buoyant plume.

Moana plume where the Fe(III) proportion increases from 54 to 74% while the Fe(II) contribution remains at ~10% and the Fe-sulfide fraction decreases from 35 to 15% (per atom basis). The Mariner plume behaves differently in that as plume elevation increases the proportion of reduced Fe species actually increases while the proportion of oxidized Fe decreases.

3.1.2. *ABE plume profile*

Individual Fe XANES spectra for the entire ABE plume profile are presented in Fig. 3, allowing for a visual comparison of the presence of various Fe chemical speciation types as a function of plume elevation. Spectra for known standards of an Fe-sulfide (pyrite), Fe(II) ($FeCl_2$), and Fe(III) (ferrihyrdrite) are included for comparison. All three Fe species are present in the near bottom background and 1.5 m samples. As plume elevation increases the proportion of Fe(II) in the samples decreases; in fact, by the time an elevation of 200 m is reached only Fe(III) and Fe-sulfide remain. This is generally consistent with the Fe chemical speciation mapping results for the ABE profile (Table 1) where the proportion of Fe-sulfide remains >35% at 3 out of 4 heights (all but 10 m), while Fe (III) varies between 33 and 78% depending on height and Fe(II) drops by 50% from 14 to 7% as height increases from 0.5 to 200 m (all % on per atom basis).

3.1.3. *Comparison of near bottom background and above plume background*

Near bottom background samples were collected for ABE and Kilo Moana vent sites. The samples were collected adjacent to the vent but out of the direct line of the buoyant plume for each. The purpose of the near bottom background samples is to define the chemical signature of materials entrained into the buoyant plume. Entrainment is an important process that mixes chemical reactants, such as dissolved oxygen and particulate organic carbon, from the near background seawater with vented fluids. Suspended materials from nearby rocks and sediments (having complex histories) are also entrained, thereby diluting particulate Fe species formed from vent fluids in the buoyant plume. In general, primary silicates found within the buoyant plume are considered entrained materials of non-hydrothermal origin because conditions for their formation are not present in the buoyant plume. In contrast, secondary phyllosilicates such as Fe(III)-bearing smectites could potentially form in plumes but the present study was not able to distinguish between secondary phyllosilicates of hydrothermal and non-hydrothermal origin.

At both sites, the concentration of background particulate Fe is approximately 50% of the 0.5 and 1.5 m plume elevation concentrations (Table 1). In contrast, the background particulate Fe concentration is higher than concentrations in the buoyant plume at 200 m elevation. In other words, the plume particulate Fe concentration decreases below that of our near-seafloor background sample. These relative particulate Fe concentrations are consistent with: (1) a strong particulate Fe background signal near the seafloor that contributes particulate Fe to the young buoyant plume; and (2) a dilute particulate Fe background signal at higher plume elevations. In future work, a depth profile of background samples could resolve this complexity.

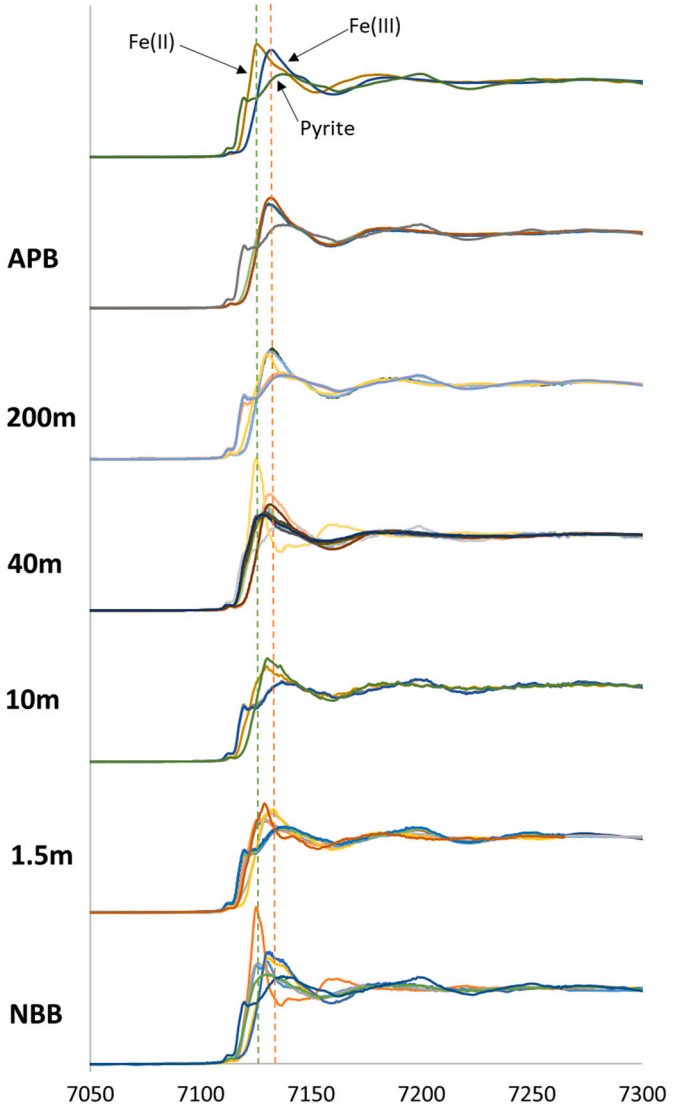

Fig. 3. Iron point X-ray absorption near edge structure (XANES) spectra showing differences in particulate Fe speciation for samples collected as the above plume background (APB), within the buoyant plume at different elevations above the vent, and a near bottom background (NBB) for the A1 vent at ABE vent field. Green and orange dotted lines represent the position of Fe(II) and Fe(III) spectra, respectively. (For interpretation of the references to colour in this figure legend, the reader is referred to the web version of this article.)

Iron chemical mapping results indicate that near bottom background samples at both sites contain a combination of oxidized and reduced species distributed across the Fe-sulfide, Fe(II), and Fe(III) bins (Table 1). The Fe(III) proportion is higher at the Kilo Moana site, where it comprises 71% of the Fe pool, compared to 50% at the ABE vent. Point XANES analysis was used to get more information about the background particulate Fe speciation. The ABE sample had equal portions of Fe-bearing primary silicates (represented by references andradite, almandine, hypersthene, and gehlenite) and non-sulfide Fe(II) (represented by references ferrous sulfate, siderite, basalt glass, ilmenite, and perovskite) which each having 34% of the total Fe in the points examined (Table S1). In comparison to ABE, the Kilo Moana sample has a greater amount of Fe-sulfide (represented by references pyrite and FeS) and mixed valence Fe(II/III) phases (represented by the reference green rust), and no detectable Fe-silicates in the two points examined (Table S1). In general, the particulate Fe background at ABE is most consistent with non-hydrothermal materials (e.g. primary silicates) while the Kilo Moana background is most consistent with re-entrainment of hydrothermal materials (e.g. Fe sulfides and oxyhydroxides) at the time and location of sampling. A description of how to interpret Fe XANES reference spectra is provided in Section 2.4.3, and the chemical formulas for reference materials, as well as the point XANES binning key are provided in Table S2.

Above plume background samples were collected at 300 m above the ABE and Kilo Moana vent sites. The purpose of the above plume background is to define the chemical signature of materials that are settling to the vent site from above. At the Kilo Moana site, the above plume background particulate Fe concentration is greater than the 200 m plume elevation sample. This suggests that the buoyant to non-buoyant plume transition was not complete at 200 m, and the 300 m sample is in fact a plume sample (Table 1). At the ABE site, the above plume background particulate Fe concentration is approximately 25% of that in the 200 m buoyant plume sample. This suggests that the above plume background sample at ABE was taken outside of the buoyant plume but perhaps included hydrothermally derived materials.

At the Kilo Moana site, the "above plume background" sample at 300 m plume elevation has proportions of Fe-sulfide, Fe(II), and Fe(III) that are similar to the 200 m sample (Table 1). This is consistent with the 300 m plume elevation being part of the buoyant plume. At the ABE site, the above plume background is 91% Fe(III) (Table 1) and the point XANES are best fit with a variety of Fe(III)-bearing oxides, oxyhydroxides, and organics (Table S1). The remaining <10% of the particulate Fe in the above plume background is attributable to the hydrothermal (represented by references pyrite and pyrrhotite) and non-hydrothermal (represented by references richterite, pigeonite, and lizardite) sources. A description of how to interpret Fe XANES reference spectra is provided in Section 2.4.3, and the chemical formulas for reference materials, as well as the point XANES binning key are provided in Table S2.

We note that there are some discrepancies between the reported values for proportions of the various Fe species between the point XANES data (Fig. 2) and the chemical mapping results (Table 1). This is to be expected and is due to both the differing analytical methods applied, as described above, and the operational realities associated with synchrotron microprobe analysis of naturally heterogeneous environmental samples. A larger investment of instrument time in these measurements–more XANES points, and more chemical map energies–would bring the two methods into full agreement for our high heterogeneity samples. At present, the complementary use of the point XANES and chemical mapping allow us to measure pFe speciation in detail, including rare species, as well as calculate relative abundances of those species.

3.2. *Mineralogy of crystalline phases*

Synchrotron microprobe X-ray diffraction (XRD) patterns were collected and analyzed using JADE peak analysis software. Fits of Merit (FOM) and elemental composition (XRF spectroscopy) was used to devise a best fit scoring system where minerals that scored a best-fit of 3 were considered as detected (details in Supporting Information). X-ray diffraction is most effective at detecting crystalline phases in our system. Phases detected by XRD on the filter-bound particles are presented in Table 2 (with phase names and idealized formulas); a subset of these phases was also detected by Fe XANES (Table 2 and Fig. 4). Fig. 4 shows the method(s) that yielded positive detection for all Fe-bearing minerals predicted by geochemical modeling. From a total of 10 Fe-bearing phases included in the model, three were detected by Fe XANES only, three more (hematite, pyrrhotite, and pyrite) were detected by XRD and Fe XANES, and the remaining 2, wurtzite and chalcopyrite, were only detected by XRD. Both pyrrhotite and wurtzite were detected by XRD at 2 out of 3 vent sites, while pyrite was the only Fe-bearing mineral detected by XRD at all 3 sites. The ABE vent site had the most XRD detected Fe minerals with 4 while Mariner and Kilo Moana had only 3 and 2 respectively (Fig. 4).

Table 2
Results from X-ray diffraction (XRD) and Fe X-ray absorption near edge structure (XANES) spectroscopy detection at all three vent sites. Minerals underlined are predicted to form by geochemical modeling (saturation index, SI = 0).

Metal sulfides & elemental sulfur	Formula	Detection mode by site		
		Kilo Moana	ABE	Mariner
Bornite	Cu_5FeS_4	XRD	–	–
Chalcocite	Cu_2S	–	XRD	–
Chalcopyrite	$CuFeS_2$	–	–	XRD
Cubanite	$CuFe(II)_2S_3$	–	XANES	XANES
Iron Titanium Sulfide	$FeTi_3S_6$	–	–	XRD
Kesterite	$Cu_2(Zn,Fe)SnS_4$	XRD	–	–
Lautite	CuAsS	XRD	XRD	–
Mackinawite	$(Fe,Ni)_{(1+x)}S$; (x = 0–0.11)	–	–	XANES
Pentlandite	$(Fe_xNi_y)_{(x+y)}S_8$; x + y = 9	–	XANES	XANES
Pyrite	FeS_2	XRD, XANES	XRD, XANES	XRD, XANES
Pyrrhotite	$Fe_{(1-x)}S$; x = 0–0.17	XANES	XANES	XANES
Rudashevskyite	(Fe,Zn)S	XRD	–	–
Sphalerite	(Zn, Fe)S	–	XRD	XRD
Stannoidite	$Cu(I,II)_8(Fe(II),Zn)_3Sn_2S_{12}$	XRD	–	–
Troilite or FeS	FeS	XANES	XRD, XANES	XANES
Wurtzite	(Zn, Fe)S	XRD	XRD	–
Elemental Sulfur	S8	–	XRD	XRD
Metal (Oxyhydr)oxides				
Akaganeite	β-FeO(OH,Cl)	–	XANES	–
Biogenic Iron Oxyhydroxide (formula unknown)		–	XANES	XANES
Chromite	$Fe(II)Cr(III)_2O_4$	–	XANES	XANES
Ferrihydrite	$Fe_2O_{3-0.5y}(OH)_y \cdot nH_2O$ y = 0–1.96; n = 0.82–1.14	XANES	XANES	XANES
Franklinite	$(Fe,Zn)_2O_4$	–	–	XRD
Goethite	α-FeOOH	XANES	XANES	XANES
Green Rust	$Fe(III)_xFe(II)_y(OH)_{3x+2y-z}(A^-)_z$; $A^- = Cl^-$; $0.5SO_4^{2-}$	XANES	XANES	XANES
Hematite	Fe_2O_3	–	XRD, XANES	–
Ilmenite	$Fe(II)TiO_3$	–	–	XANES
Lepidocrocite	γ-FeOOH	–	–	XANES
Magnetite	$Fe(II,III)_3O_4$	XANES	XANES	XANES
Perovskite	$(Ca,Fe)TiO_3$	–	XANES	XANES
Pseudobrookite	$Fe(III)_2Ti(IV)O_5$	XANES	XANES	XANES
Wustite	FeO	–	–	XANES
Sulfates, Phosphates, Carbonates & Halides				
Apatite	$Ca_5(PO_4)_3(Cl/F/OH)$	–	–	XRD
Coalingite	$Mg_{10}Fe(III)_2(OH)_{24}CO_3{\cdot}2H_2O$	–	XANES	XANES
Fluorite	CaF_2	–	–	XRD
Grattarolaite	$Fe_3(PO_4)O_3$	–	–	XRD
Halite	NaCl	–	XRD	XRD
Iron Sulfate	$FeSO_4$	–	XANES	XANES
Molysite	$FeCl_3$	–	XANES	XRD
Schulenbergite	$(Cu,Zn)_7(SO_4)_2(OH)_{10}{\cdot}3H_2O$	–	XRD	XRD
Siderite	$FeCO_3$	–	–	XANES
Silicates				
Grossular	$Ca_3Al_2(SiO_4)_3$	–	XRD	–
Akermanite	$Ca_2Mg(Si_2O_7)$	–	XRD	–
Quartz	SiO_2	–	XRD	–
Ferrosmectite	Ferruginous Smectite Swa-1[a]	XANES	–	XANES
Montmorillonite	Texas Montmorillonite STx-1[a]	–	XANES	XANES
Nontronite	Nontronite NG-1[a]	–	XANES	–
Richterite	$Na(NaCa)Mg_5Si_8O_{22}(OH)_2$	XANES	XANES	XANES
Roedderite	$Na_{1.5}K_{0.5}Mg_{3.75}Fe(II)_{1.25}Si_{12}O_{30}$	XANES	XANES	–
Augite	$(Ca,Na)(Mg,Fe,Al,Ti)(Si,Al)_2O_6$	XANES	XANES	XANES
Almandine	$Fe(II)_3Al_2(SiO_4)_3$	–	XANES	XANES
Hypersthene	$(Mg,Fe)SiO_3$	XANES	XANES	–
Chlorite	$(Mg,Fe)_3(Si,Al)_4O_{10}(OH)_2{\cdot}(Mg,Fe)_3(OH)_6$	–	XANES	–
Olivine	$(Mg,Fe)SiO_4$	–	XANES	XANES
Gehlenite	$Ca_2Al(AlSiO_7)$	–	–	XANES
Hedenbergite	$CaFe(II)Si_2O_6$	–	–	XANES

Phases in *italic* are predicted equilibrium phases (SI = 0) while phases that are underlined are predicted to be undersaturated (0 > SI ≥ -2).
[a] Clay Minerals Society source clays.

The number of mineral phases detectable by XRD in our systems is greater for Fe-sulfur compounds than for Fe (oxyhydr)oxides. For example, only one Fe (oxyhydr)oxide, hematite, was detected by XRD while 5 individual Fe—S phases were detected by XRD (Table 2). This is attributed to diffraction detecting only the more crystalline materials in our system. Additionally, a considerable number of metal sulfides (metals other than Fe), sulfates, halides, and phosphates that are detected by XRD. While various metal sulfides are detected at all 3 vent sites, the vast majority of sulfate, halide, and phosphates are detected at the Mariner site (Table 2).

3.3. Mineral precipitation predicted by reaction path modeling

Thermodynamic reaction path modeling was performed with REACT, part of the Geochemist's Workbench package. Predictions for the mineral precipitation resulting from the convective mixing of 1 kg of each of ABE, Kilo Moana or Mariner vent fluid with surrounding seawater to plume dilutions of 1:10,000 and a final mixture temperature of 2 °C are presented in Fig. S6. Quartz, dolomite, dolomite-ordered, and pyrolusite precipitation paths are predicted but are likely kinetically limited in this environment; formation of other minerals may also be kinetically limited to varying degrees. Several minerals are predicted to precipitate over a wide range of temperatures at all three sites including pyrite and hematite. For example, pyrite is predicted to form from 309 °C to approximately 30 °C in concentrations ranging from a maximum of 30 mg kg^{-1} vent fluid in the ABE reaction pathway to 200 mg kg^{-1} vent fluid in Kilo Moana and Mariner pathways. While temperature measurements at the point of sample collection within the rising plume were not generally possible during these cruises, during one profile temperatures were measured in the rising plume of A1 vent in the ABE hydrothermal field with the temperature probe of the In situ Electrochemical Analyzer system (Luther et al., 2008). Those results were used to calibrate a fluid transport model of the ABE hydrothermal plume, which indicates that the mixing and temperature reduction described in the reaction path reaches temperatures just a few degrees above background seawater within only a few meters above the vent. While the rapid pace of hydrothermal plume mixing in this system may favor precipitation of amorphous mineral phases like ferrihydrite, crystalline phases such as hematite are more prevalent in thermodynamic databases (Breier et al., 2012). Magnetite is only predicted as an equilibrium phase at the very start of the ABE reaction path at a temperature of 309 °C and a concentration of 1.2 mg kg^{-1} vent fluid.

4. Discussion

Hydrothermal plumes are globally distributed features in which the flux of elements from the subseafloor to the base of the oceanic water column is modulated. For buoyant plumes, the site-specific conditions and processes—physical, chemical, and biological—affecting the flux of elements to the deep ocean are yet to be described in a comprehensive manner through either observation or modeling. For elements such as Fe, processes occurring within plumes should determine the overall flux of Fe to the deep ocean, as well as its potential for transport and reactivity during transport. Ultimately, oceanographers seek to understand

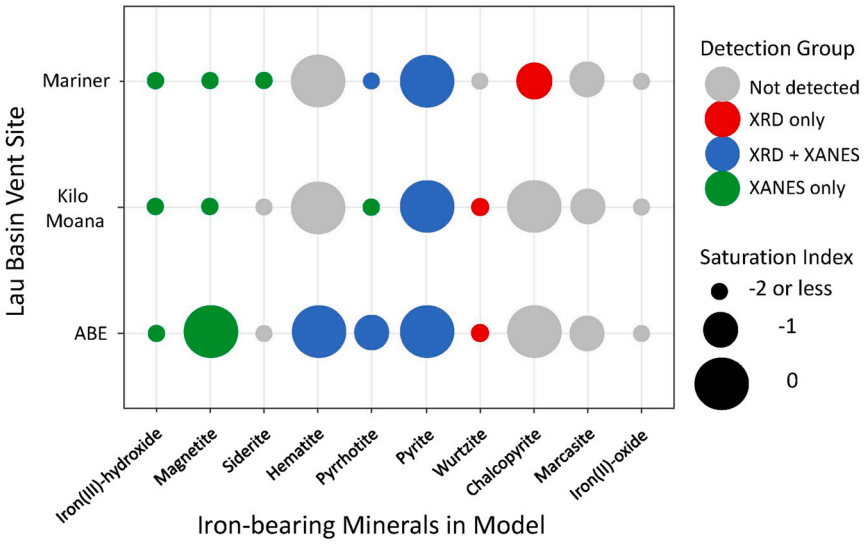

Fig. 4. Bubble plot showing the detection mode (by colour) and thermodynamic model saturation index (SI, by circle size) for Fe-bearing minerals included in the thermodynamic database according to vent field. Detection modes are: (1) not detected, ND, in grey; (2) X-ray diffraction, XRD, in red; (3) X-ray absorption near edge structure, XANES, spectroscopy, in green; and (4) both XRD and XANES in blue. The saturation index (SI) is represented by: (1) largest circles have an SI = 0, and are predicted to form in the plume by the model; and (2) smaller circles have an SI of −1 or − 2 and are not predicted to form in the plume by the model. (For interpretation of the references to colour in this figure legend, the reader is referred to the web version of this article.)

the processes controlling Fe speciation in plumes well enough to create realistic models of hydrothermal fluxes to the ocean. Therefore, in this study, we have sought to measure all forms of pFe speciation within buoyant plumes and clarify the degree to which pFe speciation is well-represented by a thermodynamic (equilibrium) modeling approach.

In the Lau Basin, end member vent chemistry varies significantly across the three vent sites examined in this study. For example, dissolved Fe concentrations range more than an order of magnitude between 0.27 mmol/kg for the ABE vent to 11.3 mmol/kg seawater at Mariner. The Kilo Moana site falls between these values with an Fe concentration of 2.5 mmol/kg (Mottl et al., 2011). In comparison, both H_2S(aq) and SiO_2 concentrations vary less with H_2S ranging from 3.6 mmol/kg at ABE to 6 and 6.2 mmol/kg at Kilo Moana and Mariner, respectively, and SiO_2 concentrations at all sites measuring between 16 and 19 mmol/kg. This results in a noticeably different Fe:S ratio at each of the three sites. The ABE vent is characterized as a high sulfur setting with 1:13 Fe:S ratio while, in contrast, Mariner is dominated by Fe with an Fe:S ratio of 2:1. Kilo Moana falls between the two with a 1:2 Fe:S ratio. Chemical mapping pFe speciation data (Table 1) show that the average Fe-sulfide % (proportion of pFe residing in a FeS mineral) is highest in the ABE plume at 39% and lowest at Mariner with 14%. It follows that Kilo Moana with the middle Fe:S ratio has 24% of Fe residing in an Fe-sulfide mineral phase. While the Mariner plume has the lowest proportion of Fe-sulfide phases, it is expected that the high concentration of total dissolved Fe at Mariner will yield the highest concentration of Fe-sulfide particles of the three sites. This is in agreement with the findings of Yucel et al. (2011) who report the highest amount of FeS_2 at the Mariner vent site (it is noted that our study used 0.8 μm filters as opposed to 0.2 μm).

4.1. Iron phases in thermodynamic equilibrium in the buoyant plume

Thermodynamic modeling predicts that the mineral magnetite (see Table 2 for phase names and formulas) should form under equilibrium conditions in the ABE buoyant plume, but not in the Kilo Moana or Mariner plumes. This discrepancy could be driven by differences in particle entrainment across the 3 vents. Magnetite was in fact detected with Fe XANES a total of three times in our buoyant plume sample set, twice at ABE and once at Kilo Moana. One observation at the ABE site was in the 200 m plume sample where 58% of the pFe in the grain examined was magnetite with the remaining Fe best represented by an Fe-substituted brucite and a phyllosilicate nontronite from our reference database. A second magnetite observation in the ABE plume occurred at 40 m plume elevation. In that case, 28% of pFe was in the form of magnetite while the remaining Fe was best represented by Fe in the form of augite (pyroxene) and perovskite (Fe substituted Ti oxide). Magnetite was also detected in the 0.5 m Kilo Moana sample where the pFe was 19% magnetite with the remaining Fe best represented by pyrite and pyrrhotite.

Hematite is predicted to form in buoyant plumes at all sites investigated: ABE, Kilo Moana, and Mariner. However, hematite was detected just once in a single sample from the ABE site at 1.5 m plume elevation. The observation was confirmed by both Fe XANES and XRD analysis. In the best-fit to the Fe XANES data, hematite accounted for 89% of pFe in a grain that also contained, or was co-located with, phases most consistent with haxonite (native Fe) and almandine (garnet).

Overall, these observations are robust in that both magnetite and hematite have unique spectral signatures and the percent attributed to each of them in the best-fits is well above conservative detection limits. While thermodynamic modeling indicates that magnetite (at ABE) and hematite (all three sites) are stable phases at equilibrium within the plume, their presence does not prove that the phases formed within the plume. Whether they formed in the plume or were entrained from non-hydrothermal sources, high stability Fe oxides, magnetite and hematite, account for only a very small proportion (< 2%) of the total pFe in the ELSC samples compared to the abundant metastable Fe (oxyhydr)oxides (see Section 4.2).

Thermodynamic modeling predicts that pyrite should form at equilibrium in all three buoyant plumes. Indeed pyrite was detected by both Fe XANES and XRD at every site and at all plume elevations, including the background samples. Pyrite is an abundant form of Fe at the ELSC and represents ~19% of all pFe as measured by Fe XANES. Pyrite has been detected in the <0.2 μm size fraction previously at both the East Pacific Rise and the ELSC (Yucel et al., 2011) and the Lau back-arc (Keith et al., 2016). Pyrite has a distinctive spectral shape in Fe XANES spectra and is one of the few Fe-bearing minerals for which inclusion in the best-fit is diagnostic for the presence of the mineral. All evidence available suggests pyrite forms in the plume, reaches equilibrium quickly, and is well represented by equilibrium modeling.

In contrast to pyrite, the sulfide mineral chalcopyrite shows poor agreement between modeling and measured observations. Chalcopyrite is predicted to form at equilibrium at both ABE and Kilo Moana, but was not detected by XRD at either site (the Fe XANES database does not contain a chalcopyrite reference). While chalcopyrite is not predicted to form at the Mariner site, it was detected with high confidence for five grains via XRD.

4.2. Iron phases out of thermodynamic equilibrium in the buoyant plume

Iron (oxyhydr)oxides are abundant and ubiquitous in the ELSC buoyant plumes and were detected at ABE, Kilo Moana, and Mariner by Fe XANES spectroscopy. Across samples from all three sites, the Fe(III) oxyhydroxides ferrihydrite and goethite account for ~17% of the pFe as detected by XANES. While Fe XANES lacks the chemical sensitivity needed to unambiguously distinguish closely related Fe (oxyhydr)oxide phases, several types of Fe (oxyhydr)oxides and related phases were selected as best-fits from the reference library indicating diversity in the phases present. Iron oxides, hydroxides, and oxyhydroxides account for ~34% of the pFe measured across all sites. As a family of phases, Fe (oxyhydr)oxides exhibit poor crystallinity and other characteristics that make them difficult to detect or undetectable by XRD. In accordance with this only two Fe (oxyhydr)oxide phases were detected in buoyant plume samples using XRD in this study (one hematite grain at ABE, one franklinite grain at Mariner).

Overall, thermodynamic modeling and direct observations yield different views of the buoyant plume for Fe (oxyhydr)oxide phases. While the thermodynamic model includes an Fe(III) hydroxide representative, goethite, ferrihydrite, green rusts, and other phases that were ultimately observed using Fe XANES are not included in the database. In all three ELSC buoyant plumes, Fe(III) hydroxide was not predicted to be present at equilibrium (saturation index $= -2$).

There are several practical issues to consider when applying an equilibrium modeling approach to Fe (oxyhydr)oxides in plumes. First, the young buoyant plume is a dynamic system and is expected to be out of equilibrium for at least some phases. Second, the diversity of phases present in the buoyant plume are not easily included in the model as representative thermodynamic parameters are lacking. Third, even if the Fe(III) hydroxide is a reasonable proxy for the family of Fe(III) (oxyhydr) oxides observed in our system, the equilibrium approach will, by definition, select the single stable phase among those included in the model database. For example, the Fe oxide hematite is included in the model, it has the lowest solubility and will draw down the Fe^{3+}_{aq} activity to the lowest value; it is predicted, therefore, to be the stable phase at equilibrium at the expense of meta-stable Fe(III) hydroxide.

While pyrrhotite was detected by Fe XANES in all three plumes, it was not predicted by thermodynamic modeling. Similar to the Fe(III) (oxyhydr)oxide phases, pyrrhotite is a family of phases and is not well distinguished from other related Fe monosulfide phases with Fe XANES. Therefore, pyrrhotite, FeS, mackinawite, troilite, pentlandite, and cubanite proportions resulting from the linear combination fits to Fe XANES spectra, are binned together in this discussion. Note that of these Fe monosulfide phases, only pyrrhotite is included in the model database. The Fe monosulfide phases account for ~14% of the pFe observed across the three vent sites, and are out of thermodynamic equilibrium in all plumes (i.e. meta-stable).

4.3. Implications for modeling hydrothermal contributions of iron to the ocean

Through the study of buoyant hydrothermal plumes at three vent sites along the Eastern Lau Spreading Center, we have determined that certain pFe species are well described by an equilibrium model (e.g. pyrite), while others are not (e.g. phases within the Fe monosulfide and Fe (oxyhydr)oxide families). Here, we use the lessons learned from this study to propose several best-practices that should help our research community build a foundation for modeling hydrothermal Fe fluxes to the ocean. Our recommendations for future work span: (1) field studies; (2) analytical observations; and (3) model development.

Quantifying hydrothermal fluxes to the deep ocean, as well as long range transport potential and bioavailability, will require additional field expeditions to hydrothermal vent systems that focus on a mass balance approach to key elements in the dissolved and solid (e.g. colloidal and particulate size classes) phases. Elemental budgets at different locations within the plume system—buoyant, near-field neutrally buoyant, and far-field neutrally buoyant—should improve our understanding of net fluxes at threshold length scales from vents. The international GEOTRACES program has recently revealed that submarine hydrothermal venting can, indeed, impact global-scale ocean biogeochemistry over 100–1000 km length scales in every ocean basin (German et al., 2016). Detailed work across GEOTRACES sections has also revealed, however, that processes critical to setting the flux from hydrothermal venting to the ocean occurs on shorter length scales (0–100 km) that are beyond the resolution of GEOTRACES sections (Fitzsimmons et al., 2017). In addition to mass balance, concentrations of elements within specific size-classes (e.g. soluble, colloidal, and particulate; e.g. ((Fitzsimmons and Boyle, 2014)) should be routinely measured, as well as chemical speciation (Toner et al., 2015) and isotopic composition (Fitzsimmons et al., 2017) of key elements within each size-class. Together, these observations will describe transport potential, relevant reactions and processes, and bioavailability. While our knowledge of the range of possible processes affecting hydrothermal fluxes, particularly of Fe, has increased in the past 15 years (Bennett et al., 2008; Cron et al., 2020; Fitzsimmons et al., 2017; Gartman and Findlay, 2020; Hoffman et al., 2018; Li et al., 2014; Lough et al., 2019; Sander and Koschinsky, 2011; Sander et al., 2007; (Toner et al., 2009); Yucel et al., 2011), our understanding of which processes are important under different venting scenarios is nascent. Future field expeditions should therefore aim to explore sites representing a diversity of site-specific conditions to better capture the full range of processes active in plumes that modulate fluxes.

Given the overall importance of precipitation-dissolution, aggregation, and sorption reactions in hydrothermal plumes, particularly for elements such as Fe, we focus our attention here on analytical recommendations for solid-state chemistry. The complexity and heterogeneity of hydrothermal plume solid-state chemistry has been demonstrated using a variety of analytical approaches (Breier et al., 2012; Feely et al., 1990; Findlay et al., 2019; Gartman et al., 2019; Gartman et al., 2014; Klevenz et al., 2011; Toner et al., 2009b). To date, the most comprehensive view of plume solid-state chemistry (organic, inorganic, crystalline, noncrystalline, and multiple elements) has been gained using a suite of X-ray microscopy and microprobe tools with X-ray diffraction and absorption spectroscopy detection modes (as reviewed by (Toner et al., 2015)). While the number of vents investigated to date is low, measurements show that hydrothermal solids in the particulate size fraction are composed of inorganic and organic phases, including biota and biotic fragments, with inorganic components spanning a wide continuum of poorly ordered to well crystalline phases (e.g. (Breier et al., 2012; Cron et al., 2020; Fitzsimmons et al., 2017; Hoffman et al., 2018; (Toner et al., 2009); Toner et al., 2012b)). For the three ELSC vents examined here, we demonstrate the necessity of measuring pFe chemistry with analytical tools that capture both crystalline (XRD) and poorly crystalline (XANES) phases. The primary pFe phase detected by XRD is pyrite which accounts for ~19% of the Fe in the samples (per atom basis). In contrast, the most abundant type of pFe observed, the meta-stable Fe (oxyhydr)oxide phases, are undetectable with XRD. This is significant given that the Fe (oxyhydr)oxide phases (not counting hematite and magnetite) account for ~33% of the pFe (per atom basis). Similarly, the Fe monosulfide phases are poorly detected by XRD and account for ~14% of the Fe present on a per atom basis. A suite of analytical approaches that can detect Fe phases with differing amounts of crystallinity is critical to gaining a complete picture of the solid-state chemistry of plume particles.

Here we have used a reaction path thermodynamic modeling approach that allows hydrothermal vent fluids to come to equilibrium under different dilution and temperature conditions, mimicking a rapidly cooling and diluting plume. Our findings, from this study and others (Breier et al., 2012), reveal important mismatches between measured observations and model calculations and demonstrate that disequilibrium is strong within buoyant plumes for certain pFe phases.

The main solid phases in the particulate size-class that are not accounted for in equilibrium modeling are also the phases that are not detectable by X-ray and electron diffraction analysis. The Fe (oxyhydr)oxide and Fe monosulfide families of phases are important components of the pFe pool that are at present poorly represented by any equilibrium modeling approach. The development of kinetic models and expansion of solid phases included in thermodynamic databases is expected to provide a path forward in this key area of research.

Declaration of Competing Interest

The authors declare that they have no known competing financial interests or personal relationships that could have appeared to influence the work reported in this paper.

Acknowledgments

We thank Chief Scientists Charles Fisher, Anna-Louise Reysenbach, George Luther, and Peter Girgus, the *ROV Jason II* team (dives J2-421 to J2-430, and J2-434 to J2-443), and the crews of the *R/V Thompson* (cruises TN235 and TN236). The research was supported by funds from the National Science Foundation's Ridge 2000 program (BMT OCE-1037991; JAB OCE-1038055; GJD OCE-1038006; OCE-1851007). We thank Katrina Edwards and Sheri White for fieldwork support. We thank Matthew Marcus and Sirine Fakra for synchrotron support at the Advanced Light Source (BL 10.3.2 and 5.3.2), as well as Sarah Nicholas, Brandi Cron Kammermans, and Teng Zeng for assistance in synchrotron data collection. The Advanced Light Source is supported by the Director, Office of Science, Office of Basic Energy Sciences, of the U.S. Department of Energy under Contract No. DE-AC02-05CH11231. We acknowledge and honor the indigenous communities native to the Twin Cities, Minnesota region where the University of Minnesota now resides on the ancestral land of the Wahpekute (Dakota), Anishinabewaki, and Očeti Šakówiŋ (Sioux) peoples. We wish to recognize the people of the Sioux tribe as the ongoing caretakers of this land.

Appendix A. Supplementary data

Supplementary data to this article can be found online at https://doi.org/10.1016/j.chemgeo.2020.120018.

References

Anantharaman, K., Breier, J.A., Sheik, C.S., Dick, G.J., 2013. Evidence for hydrogen oxidation and metabolic plasticity in widespread deep-sea sulfur-oxidizing bacteria. Proc. Natl. Acad. Sci. U. S. A. 110, 330–335.

Anantharaman, K., Duhaime, M.B., Breier, J.A., Wendt, K., Toner, B.M., Dick, G.J., 2014. Sulfur oxidation genes in diverse deep-sea viruses. Science 344, 757–760.

Bargar, J.R., Tebo, B.M., Villinski, J.E., 2000. In situ characterization of Mn(II) oxidation by spores of the marine *Bacillus* sp. strain SG-1. Geochim. Cosmochim. Acta 64, 2775–2778.

Bennett, S.A., Achterberg, E.P., Connelly, D.P., Statham, P.J., Fones, G.R., German, C.R., 2008. The distribution and stabilisation of dissolved Fe in deep-sea hydrothermal plumes. Earth Planet. Sci. Lett. 270, 157–167.

Bethke, C.M., 2007. Geochemical and Biogeochemical Reaction Modeling. Cambridge University Press, Cambridge, UK.

Bezos, A., Escrig, S., Langmuir, C.H., Michael, P.J., Asimow, P.D., 2009. Origins of chemical diversity of back-arc basin basalts: a segment-scale study of the Eastern Lau Spreading Center. J. Geophys. Res.-Solid Earth 114.

Bowers, T.S., Taylor, H.P., 1985. An integrated chemical and stable-isotope model of the origin of midocean ridge hot-spring systems. J. Geophys. Res. Solid Earth Planets 90, 2583–2606.

Bowie, A.R., Townsend, A.T., Lannuzel, D., Remenyi, T.A., van der Merwe, P., 2010. Modern sampling and analytical methods for the determination of trace elements in marine particulate material using magnetic sector inductively coupled plasma-mass spectrometry. Anal. Chim. Acta 676, 15–27.

Breier, J.A., Rauch, C.G., McCartney, K., Toner, B.M., Fakra, S.C., White, S.N., German, C.R., 2009. A suspended-particle rosette multi-sampler for discrete biogeochemical sampling in low-particle-density waters. In: Deep-Sea Research Part I-Oceanographic Research Papers 56, pp. 1579–1589.

Breier, J.A., Toner, B.M., Fakra, S.C., Marcus, M.A., White, S.N., Thurnherr, A.M., German, C.R., 2012. Sulfur, sulfides, oxides and organic matter aggregated in submarine hydrothermal plumes at 9° 50' N East Pacific rise. Geochim. Cosmochim. Acta 88, 216–236.

Campbell, A.C., 1991. Mineralogy and chemistry of marine particles by synchrotron X-ray spectroscopy, Mossbauer spectroscopy, and plasma-mass spectrometry. In: Hurd, D.C., Spencer, D.W. (Eds.), Marine Particles: Analysis and Characterization. American Geophysical Union, Washington D.C., pp. 375–390

Cleverley, J.S., Bastrakov, E.N., 2005. K2GWB: Utility for generating thermodynamic data files for the Geochemist's Workbench® at 0–1000°C and 1–5000bar from UT2K and the UNITHERM database. Comput. Geosci. 31, 756–767.

Conrad, R., Seiler, W., 1988. Methane and hydrogen in seawater (Atlantic Ocean). In: Deep Sea Research Part A. Oceanographic Research Papers 35, pp. 1903–1917.

Cowen, J.P., Massoth, G.J., Baker, E.T., 1986. Bacterial scavenging of Mn and Fe in a mid- to far-field hydrothermal particle plume. Nature 322, 169–171.

Cron, B.R., Sheik, C.S., Kafantaris, F.-C.A., Druschel, G.K., Seewald, J.S., German, C.R., Dick, G.J., Breier, J.A., Toner, B.M., 2020. Dynamic biogeochemistry of the particulate sulfur pool in a buoyant deep-sea hydrothermal plume. ACS Earth Space Chem. 4, 168–182.

Drummond, S.E., 1981. Boiling and Mixing of Hydrothermal Fluids: Chemical Effects on Mineral Precipitation. Pennsylvania State University, University Park, PA.

Estapa, M.L., Breier, J.A., German, C.R., 2015. Particle dynamics in the rising plume at Piccard hydrothermal field, Mid-Cayman rise. Geochem. Geophys. Geosyst. 16, 2762–2774.

Evans, G.N., Tivey, M.K., Seewald, J.S., Wheat, C.G., 2017. Influences of the Tonga Subduction Zone on seafloor massive sulfide deposits along the Eastern Lau Spreading Center and Valu Fa Ridge. Geochim. Cosmochim. Acta 215, 214–246.

Feely, R.A., Lewison, M., Massoth, G.J., Rober-Baldo, G., Lavelle, J.W., Byrne, R.H., Damm, K.L.V., Curl, H.C., J., 1987. Composition and dissolution of black smoker particulates from active vents on the Juan de Fuca Ridge. J. Geophys. Res. 92, 11347–11363.

Feely, R.A., Massoth, G.J., Baker, E.T., Cowen, J.P., Lamb, M.F., Krogslund, K.A., 1990. The effect of hydrothermal processes on midwater phosphorus distributions in the northeast Pacific. Earth Planet. Sci. Lett. 96, 305–318.

Feely, R.A., Gendron, J.F., Baker, E.T., Lebon, G.T., 1994. Hydrothermal plumes along the East Pacific rise, 8°40 to 11°50: particle distribution and composition. Earth Planet. Sci. Lett. 128, 19–36.

Ferrini, V.L., Tivey, M.K., Carbotte, S.M., Martinez, F., Roman, C., 2008. Variable morphologic expression of volcanic, tectonic, and hydrothermal processes at six hydrothermal vent fields in the Lau back-arc basin. Geochem. Geophys. Geosyst. 9.

Findlay, A.J., Estes, E.R., Gartman, A., Yucel, M., Kamyshny, A., Luther, G.W., 2019. Iron and sulfide nanoparticle formation and transport in nascent hydrothermal vent plumes. Nat. Commun. 10.

Fitzsimmons, J.N., Boyle, E.A., 2014. Assessment and comparison of Anopore and cross flow filtration methods for the determination of dissolved iron size fractionation into soluble and colloidal phases in seawater. Limnol. Oceanogr. Methods 12, 244–261.

Fitzsimmons, J.N., John, S.G., Marsay, C.M., Hoffman, C.L., Nicholas, S.L., Toner, B.M., German, C.R., Sherrell, R.M., 2017. Iron persistence in a distal hydrothermal plume supported by dissolved-particulate exchange. Nat. Geosci. 10, 195–201.

Gartman, A., Findlay, A.J., 2020. Impacts of hydrothermal plume processes on oceanic metal cycles and transport. Nat. Geosci. 13, 396–402.

Gartman, A., Findlay, A.J., Luther III, G.W., 2014. Nanoparticulate pyrite and other nanoparticles are a widespread component of hydrothermal vent black smoker emissions. Chem. Geol. 366, 32–41.

Gartman, A., Findlay, A.J., Hannington, M., Garbe-Schonberg, D., Jamieson, J.W., Kwasnitschka, T., 2019. The role of nanoparticles in mediating element deposition and transport at hydrothermal vents. Geochim. Cosmochim. Acta 261, 113–131.

German, C.R., Seyfried Jr., W.E., 2014. Hydrothermal Processes, Treatise on Geochemistry. Elsevier, pp. 191–233.

German, C.R., Bennett, S.A., Connelly, D.P., Evans, A.J., Murton, B.J., Parson, L.M., Prien, R.D., Ramirez-Llodra, E., Jakuba, M., Shank, T.M., Yoerger, D.R., Baker, E.T., Walker, S.L., Nakamura, K., 2008. Hydrothermal activity on the southern Mid-Atlantic Ridge: tectonically- and volcanically-controlled venting at 4-5 degrees S. Earth Planet. Sci. Lett. 273, 332–344.

German, C.R., Casciotti, K.A., Dutay, J.-C., Heimburger, L.E., Jenkins, W.J., Measures, C. I., Mills, R.A., Obata, H., Schlitzer, R., Tagliabue, A., Turner, D.R., Whitby, H., 2016. Hydrothermal impacts on trace element and isotope ocean biogeochemistry. Phil. Trans. R. Soc. A 374, 20160035.

Govindarajan, A.F., 1994. Compilation of working values and sample description for 383 geostandards. Geostand. Geoanal. Res. 18, 1639–4488.

Hammersley, A.P., Svensson, S.O., Hanfland, M., Fitch, A.N., Hausermann, D., 1996. Two-dimensional detector software: from real detector to idealized image or two-theta scan. High Pressure Res. 14, 235–248.

Hansel, C.M., Benner, S.G., Neiss, J., Dohnalkova, A., Kukkadapu, R.K., Fendorf, S., 2003. Secondary mineralization pathways induced by dissimilatory iron reduction of ferrihydrite under advective flow. Geochim. Cosmochim. Acta 67, 2977–2992.

Helgeson, H.C., 1969. Thermodynamics of hydrothermal systems at elevated temperatures and pressures. Am. J. Sci. 267, 729.

Helgeson, H.C.K., Kirkham, D.H., 1974. Theoretical prediction of the thermodynamic behavior of aqueous electrolytes at high pressures and temperatures; I, Summary of the thermodynamic/electrostatic properties of the solvent. Am. J. Sci. 1089–1198.

Helgeson, H.C.D., Delany, J.M., Nesbitt, H.W., Bird, D.K., 1978. Summary and critique of the thermodynamic properties of rock-forming minerals. Am. J. Sci. 1–129.

Hoffman, C.L., Nicholas, S.L., Ohnemus, D.C., Fitzsimmons, J.N., Sherrell, R.M., German, C.R., Heller, M.I., Lee, J.-M., Lam, P.J., Toner, B.M., 2018. Near-field iron and carbon chemistry of non-buoyant hydrothermal plume particles, Southern East Pacific rise 15oS. Mar. Chem. 201, 183–197.

Hoffman, C.L., Schladweiler, C.S., Seaton, N.C.A., Nicholas, S.L., Fitzsimmons, J.N., Sherrell, R.M., German, C.R., Lam, P.J., Toner, B.M., 2020. Diagnostic morphology and solid-state chemical speciation of hydrothermally derived particulate Fe in a long-range dispersing plume. ACS Earth Space Chem. 4, 1831–1842.
Jacobs, A.M., Harding, A.J., Kent, G.M., 2007. Axial crustal structure of the Lau back-arc basin from velocity modeling of multichannel seismic data. Earth Planet. Sci. Lett. 259, 239–255.
Janecky, D.R., Seyfried, W.E., 1984. Formation of massive sulfide deposits on oceanic ridge crests – Incremental reaction models for mixing between hydrothermal solutions and seawater. Geochim. Cosmochim. Acta 48, 2723–2738.
Jiang, H.S., Breier, J.A., 2014. Physical controls on mixing and transport within rising submarine hydrothermal plumes: A numerical simulation study. In: Deep-Sea Research Part I-Oceanographic Research Papers 92, pp. 41–55.
Johnson, J.W., Oelkers, E.H., Helgeson, H.C., 1992. SUPCRT92 - a softward package for calculating the standard molal thermodynamic properties of minerals, gases, aqueous species, and reactions from 1-bar to 5000-bar and 0-degrees-C to 1000-degrees-C. Comput. Geosci. 18, 899–947.
Keith, M., Häckel, F., Haase, K.M., Schwarz-Schampera, U., Klemd, R., 2016. Trace element systematics of pyrite from submarine hydrothermal vents. Ore Geol. Rev. 72, 728–745.
Klevenz, V., Bach, W., Schmidt, K., Hentscher, M., Koschinsky, A., Petersen, S., 2011. Geochemistry of vent fluid particles formed during initial hydrothermal fluid-seawater mixing along the Mid-Atlantic Ridge. Geochem. Geophys. Geosyst. 12.
Lam, P.J., Lee, J.-M., Heller, M.I., Mehic, S., Xiang, Y., Bates, N.R., 2018. Size-fractionated distributions of suspended particle concentration and major phase composition from the U.S. GEOTRACES Eastern Pacific Zonal Transect (GP16). Mar. Chem. 201, 90–107.
Lee, J.-M., Heller, M.I., Lam, P.J., 2018. Size distribution of particulate trace elements in the U.S. GEOTRACES Eastern Pacific Zonal Transect (GP16). Mar. Chem. 201, 108–123.
Li, M., Toner, B.M., Baker, B.J., Breier, J.A., Sheik, C.S., Dick, G.J., 2014. Microbial iron uptake as a mechanism for dispersing iron from deep-sea hydrothermal vents. Nat. Commun. 5.
Lough, A.J.M., Connelly, D.P., Homoky, W.B., Hawkes, J.A., Chavagnac, V., Castillo, A., Kazemian, M., Nakamura, K., Araki, T., Kaulich, B., Mills, R.A., 2019. Diffuse Hydrothermal Venting: a Hidden source of Iron to the Oceans. Front. Mar. Sci. 6.
Luther, G.W., Glazer, B.T., Ma, S.F., Trouwborst, R.E., Moore, T.S., Metzger, E., Kraiya, C., Waite, T.J., Druschel, G., Sundby, B., Taillefert, M., Nuzzio, D.B., Shank, T.M., Lewis, B.L., Brendel, P.J., 2008. Use of voltammetric solid-state (micro) electrodes for studying biogeochemical processes: laboratory measurements to real time measurements with an in situ electrochemical analyzer (ISEA). Mar. Chem. 108, 221–235.
Marcus, M.A., MacDowell, A., Celestre, R., Manceau, A., Miller, T., Padmore, H.A., Sublett, R.E., 2004. Beamline 10.3.2 at ALS: a hard X-ray microprobe for environmental and material sciences. J. Synchrotron Radiat. 11, 239–247.
Marcus, M.A., Westphal, A.J., Fakra, S., 2008. Classification of Fe-bearing species from K-edge XANES data using two-parameter correlation plots. J. Synchrotron Radiat. 15, 463–468.
Martinez, F., Taylor, B., Baker, E.T., Resing, J.A., Walker, S.L., 2006. Opposing trends in crustal thickness and spreading rate along the back-arc Eastern Lau Spreading Center: Implications for controls on ridge morphology, faulting, and hydrothermal activity. Earth Planet. Sci. Lett. 245, 655–672.
Mayhew, L.E., Webb, S.M., Templeton, A.S., 2011. Microscale imaging and identification of Fe oxidation state, speciation, and distribution in complex geological media. Environ. Sci. Technol. 45, 4468–4472.
McCollom, T.M., 2000. Geochemical constraints on primary productivity in submarine hydrothermal vent plumes. Deep-Sea Res. 47, 85–101.
McCollom, T.M., Shock, E.L., 1997. Geochemical constraints on chemolithoautotrophic metabolism by microorganisms in seafloor hydrothermal systems. Geochim. Cosmochim. Acta 61, 4375–4391.
Mottl, M.J., McConachy, T.F., 1990. Chemical processes in buoyant hydrothermal plumes on the East Pacific rise near 21 ° N. Geochim. Cosmochim. Acta 54, 1911–1927.
Mottl, M.J., Seewald, J.S., Wheat, C.G., Tivey, M.K., Michael, P.J., Proskurowski, G., McCollom, T.M., Reeves, E., Sharkey, J., You, C.F., Chan, L.H., Pichler, T., 2011. Chemistry of hot springs along the Eastern Lau Spreading Center. Geochim. Cosmochim. Acta 75, 1013–1038.
Nicholas, S.L., Erickson, M.L., Woodruff, L.G., Knaeble, A.R., Marcus, M.A., Lynch, J.K., Toner, B.M., 2017. Solid-phase arsenic speciation in aquifer sediments: a micro-X-ray absorption spectroscopy approach for quantifying trace-level speciation. Geochim. Cosmochim. Acta 211, 228–255.
Ravel, B., Newville, M., 2005. Athena, Artemis, Hephaestus: data analysis for X-ray absorption spectroscopy using IFEFFIT. J. Synchrotron Radiat. 12, 537–541.
Robie, R.A.H., Hemingway, B.S., Fisher, J.R., 1979. Thermodynamic properties of minerals and related substances at 298.15 K and 1 Bar (10 Pascals) pressure and at higher temperatures. In: US Geological Survey 1979, Bulletin, p. 456.
Saccocia, P.J., Seyfried, W.E., 1994. The solubility of chlorite solid solutions in 3.2 wt% NaCl fluids from 300–400°C, 500 bars. Geochim. Cosmochim. Acta 58, 567–585.
Sander, S.G., Koschinsky, A., 2011. Metal flux from hydrothermal vents increased by organic complexation. Nat. Geosci. 4, 145–150.
Sander, S.G., Koschinsky, A., Massoth, G.J., Stott, M., Hunter, K.A., 2007. Organic complexation of copper in deep-sea hydrothermal vent systems. Environ. Chem. 4, 81–89.
Seewald, J.M., McCollom, T., Proskurowski, G., Reeves, E., Mottl, M., Sharkey, J., Wheat, C.G., Tivey, M., 2005. Aqueous volatiles in Lau Basin hydrothermal fluids. In: American Geophysical Union Fall Meeting, pp. T31A–0478.
Shafer, M.M., Toner, B.M., Overdier, J., Schauer, J.J., Fakra, S.C., Hu, S., Herner, J.D., Ayala, A., 2011. Chemical speciation of vanadium in particulate matter emitted from diesel vehicles and urban atmospheric aerosols. Environ. Sci. Technol. 46, 189–195.
Sheik, C.S., Anantharaman, K., Breier, J.A., Sylvan, J.B., Edwards, K.J., Dick, G.J., 2015. Spatially resolved sampling reveals dynamic microbial communities in rising hydrothermal plumes across a back-arc basin. ISME J. 9, 1434–1445.
Shock, E.L., Helgeson, H.C., 1990. Calculation of the thermodynamic and transport properties of aqueous species at high pressures and temperatures: Standard partial molal properties of organic species. Geochim. Cosmochim. Acta 54, 915–945.
Shock, E.L., Helgeson, H.C., Sverjensky, D.A., 1989. Calculation of the thermodynamic and transport properties of aqueous species at high pressures and temperatures: Standard partial molal properties of inorganic neutral species. Geochim. Cosmochim. Acta 53, 2157–2183.
Shock, E.L., Sassani, D.C., Willis, M., Sverjensky, D.A., 1997. Inorganic species in geologic fluids: Correlations among standard molal thermodynamic properties of aqueous ions and hydroxide complexes. Geochim. Cosmochim. Acta 61, 907–950.
Speer, K.G., Helfrich, K.R., 1995. Hydrothermal plumes: A review of flow and fluxes. In: Parson, L.M., Walker, C.L., Dixon, D.R. (Eds.), Hydrothermal Vents and Processes. Geological Society Special Publications, pp. 373–385.
Sverjensky, D.A., Shock, E.L., Helgeson, H.C., 1997. Prediction of the thermodynamic properties of aqueous metal complexes to 1000°C and 5 kb. Geochim. Cosmochim. Acta 61, 1359–1412.
Talley, L.D., 2007. Hydrographic atlas of the world ocean circulation experiment (WOCE). In: Sparrow, M., Chapman, P., Gould, J. (Eds.), Volume 2: Pacific Ocean, Southampton, UK.
Toner, B.M., Fakra, S.C., Manganini, S.J., Santelli, C.M., Marcus, M.A., Moffett, J.W., Rouxel, O., German, C.R., Edwards, K.J., 2009. Preservation of Iron(II) by Carbon-Rich Matrices in Hydrothermal Plumes. Nature Geoscience 2, 197–201.
Toner, Brandy M., Nicholas, Sarah L., Jill, Coleman Wasik K., 2014. Scaling up: Fulfilling the promise of X-ray microprobe for biogeochemical research. Environmental Chemistry 11, 4–9. https://doi.org/10.1071/EN13162.
Toner, B.M., Santelli, C.M., Marcus, M.A., Wirth, R., Chan, C.S., McCollom, T.M., Bach, W., Edwards, K.J., 2009b. Biogenic iron oxyhydroxide formation at Mid-Ocean Ridge hydrothermal vents: Juan de Fuca Ridge. Geochim. Cosmochim. Acta 73, 388–403.
Toner, B.M., Berquo, T.S., Michel, F.M., Sorensen, J.V., Templeton, A.S., Edwards, K.J., 2012a. Mineralogy of iron microbial mats from Loihi Seamount. Front. Microbiol. Chem. 3, 1–18.
Toner, B.M., Marcus, M.A., Edwards, K.J., Rouxel, O., German, C.R., 2012b. Measuring the form of iron in hydrothermal plume particles. Oceanography 25, 209–212.
Toner, Brandy M., Fakra, Sirine C., Manganini, Steven J., Marcus, Matthew M., Moffett, James W., Rouxel, Olivier, German, Christopher R., Edwards, Katrina J., 2009. Preservation of Iron(II) by Carbon-Rich Matrices in Hydrothermal Plumes. Nature Geoscience 2, 197–201. https://doi.org/10.1038/ngeo433.
Toner, B.M., German, C.R., Dick, G.J., Breier, J.A., 2015. Deciphering the complex chemistry of deep-ocean particles using complementary synchrotron X-ray microscope and microprobe instruments. Acc. Chem. Res. 49, 128–137.
Von Damm, K.L., Edmond, J.M., Grant, B., Measures, C.I., Walden, B., Weiss, R.F., 1985. Chemistry of submarine hydrothermal solutions at 21 °N, East Pacific rise. Geochim. Cosmochim. Acta 49, 2197–2220.
Wagman, D.D.E., Evans, W.H., Parker, V.B., Schumm, R.H., Halow, I., Balley, S.M., Churney, K.L., 1982. NBS Tables of Chemical Thermodynamic Properties: Selected Values for Inorganic and C1 and C2 Organic Substances in SI Units. American Chemical Society and the American Institute of Physics for the National Bureau of Standards, Washington, D.C.
Yu, J.Y., Park, M., Kim, J., 2002. Solubilities of synthetic schwertmannite and ferrihydrite. Geochem. J. 36, 119–132.
Yucel, M., Gartman, A., Chan, C.S., Luther, George W., I., 2011. Hydrothermal vents as a kinetically stable source of iron-sulphide-bearing nanoparticles to the ocean. Nat. Geosci. 4, 367–371.
Zeng, T., Arnold, W.A., Toner, B.M., 2013. Microscale characterization of sulfur speciation in lake sediments. Environ. Sci. Technol. 47, 1287–1296.